Radiative damping and interference in the resonance structure of the electron-impact excitation cross sections for Ti^{20+}

T. W. Gorczyca, F. Robicheaux, and M. S. Pindzola
Department of Physics, Auburn University, Auburn, Alabama 36849

N. R. Badnell
Department of Physics and Applied Physics, University of Strathclyde, Glasgow, G4 0NG, United Kingdom
(Received 28 March 1995)

We have performed R-matrix calculations for the electron-impact excitation of a highly charged ion in which an optical potential is included to allow for radiative damping of intermediate resonance states. The present case considered is that of electrons incident on Ti^{20+} ions. Comparisons with undamped R-matrix calculations, distorted-wave calculations, and experimental measurement are made. The radiative optical potential accounts for significant damping of high-n resonances. Configuration interaction between resonances, which is automatically incorporated in the R-matrix method but usually omitted in the implementation of distorted-wave techniques, was found to increase the resonance contributions considerably. Our radiative-damped R-matrix cross sections show fairly good agreement with the resonance profile obtained from electron beam ion trap measurements [S. Chantrenne *et al.*, Phys. Rev. Lett. **69**, 265 (1992)]. This system demonstrates the necessity for simultaneously including radiative-damping and interfering-resonance effects within electron–highly charged ion scattering calculations.

PACS number(s): 34.80.Kw

I. INTRODUCTION

The collision of electrons with atomic ions constitutes a fundamental process in laboratory and astrophysical plasmas. Electron-impact excitation cross sections in particular serve as important diagnostics for determining the temperature and density of a plasma [1,2]. This excitation may be significantly enhanced by resonance processes [3], whereby the target ion is excited, temporarily captures the incident electron into the resonant state, and then autoionizes. There are two important phenomena that affect the determination of this resonance contribution. The first is radiative damping [4]. When the temporary resonant state, consisting of the target ion plus incident electron, is formed, there is also the possibility that a photon can be spontaneously emitted. This leads to a reduction in the resonance contribution seen in the excitation cross sections, since the captured resonance state has this radiative decay pathway in addition to the autoionization pathways to the ground or excited continua. At lower ionization stages, this radiative rate A_r is typically several orders of magnitude lower than the autoionization rate A_a, so that this effect is negligible. But as the residual charge Z on the target ion increases, the radiative rate, which scales like Z^4 for $\Delta n>0$ core transitions, eventually becomes comparable to the autoionization rate, which does not scale with Z. Thus the inclusion of this alternate decay pathway is essential when studying excitation of highly charged ions.

A second important phenomenon is interference. In general, the resonance process due to capture into one autoionizing configuration cannot be considered independent of either the direct excitation process or the capture into a neighboring resonance state. In the first case, the interference of a resonance with the direct, or background, cross section can lead to an asymmetric profile [5]. The effect of this type of interference in most cases disappears when the cross section is thermally averaged. Interference between two adjacent resonances, on the other hand, may have a drastic effect on the resonance profile. The two may interfere through a common continuum, but this requires a small energy separation, and is of order V^2 in perturbation theory (V is the electron-electron interaction potential $V=1/r_{12}$). More important is the direct configuration interaction (CI) between two resonances, which is of order V and can be appreciable even when the resonances do not completely overlap. A recent study of excitation in Mg-like ions [6] showed that in some cases, CI effects lead to huge enhancements in the resonance profile. Interference through a common continuum was not appreciable, however.

One method often used to calculate the resonance contribution to electron-impact excitation is the independent-processes isolated-resonance distorted-wave (IPIRDW) approximation [7–10]. In this perturbative method, inclusion of radiative-damping effects is straightforward. However, the interference effects discussed above, while possible to include for two selected resonances [6], are difficult to implement within a general scheme for complete Rydberg series.

The R-matrix method [11,12], on the other hand, uses a close-coupling formalism whereby all orders of interference are automatically taken into account. The only drawback to this method had been that the existing formulation for including radiative damping [4] was either impractical for complex cases [13] or incomplete [14,15]. Recently, we have outlined a general formulation for the inclusion of radiative-damping effects in the close-coupling equations [16]. It was shown how this R-matrix method, using a radiative optical

potential, was successful in calculating cross sections for dielectronic recombination and photoionization of certain atomic ions. The primary purpose of this paper is to investigate the use of this method for radiative damping of resonances in the electron-impact excitation of highly charged ions, in a case where interference effects are expected to be important.

The collision of electrons with heliumlike Ti^{20+} ions represents a relatively simple system for which the inclusion of both radiative-damping and interference effects are required. The residual charge $Z=20$ is so large that the radiative decay rates of resonances are comparable to the autoionization rates. And since there are multiple Rydberg series, resonance overlap is inevitable. Measurements of the excitation cross sections for electrons incident on Ti^{20+} have been performed at the Electron Beam Ion Trap (EBIT) [17]. These results were compared to distorted-wave calculations [18], and certain discrepancies between the theoretical and experimental resonance profiles were noticed. We reinvestigated this collisional excitation process in order to see whether or not interference effects, which were omitted in those calculations [18], could be attributed to the existing discrepancy between theory and experiment.

The remainder of the paper is organized in the following manner. In the next section, we outline the present numerical techniques used. Specifically, we describe the inclusion of radiative damping within the present R-matrix calculations, and discuss the CI between resonances within the distorted-wave method. We then present a results section which compares (1) R-matrix calculations with and without radiative damping, (2) distorted-wave calculations with and without CI between resonances, and (3) radiative-damped R-matrix calculations with the EBIT experiment. We conclude with a summary of the present work.

II. NUMERICAL METHODS

Our present method for treating electron-ion collisions utilizes the R-matrix method [11,12]. Specifically, we use the latest version [19] of programs coded for the Iron Project [20]. These codes utilize an intermediate coupling scheme to incorporate a Breit-Pauli Hamiltonian into the R-matrix method [21,22], which allows for the inclusion of spin-orbit, mass-velocity, and one-body Darwin potentials. The portion of this computer package known as STGF [23], which computes the final R-matrix, and calculates the outer-region solutions using asymptotic methods of Seaton [23–25], has been extensively modified to include a nonlocal, energy-dependent radiative optical potential [16]. The R-matrix is first obtained by computing eigenvalues ϵ_α and eigenvectors of the full Hamiltonian, yielding the following expression at all values of the energy E:

$$R_{ij}(E)=\frac{1}{2r_a}\sum_\alpha \frac{w_{i\alpha}w_{j\alpha}}{\epsilon_\alpha-E} \quad . \tag{1}$$

Here $w_{i\alpha}$ are the values of the channel eigenvectors on the surface of the R-matrix "box," $r=r_a$, which is chosen to be large enough that all of the atomic orbitals required for the target states are contained within this region. Outside of the R-matrix box ($r_a<r<\infty$), the wave function is instead a solution to the asymptotic equations

$$\left(-\frac{1}{2}\frac{d^2}{dr^2}+\frac{\ell_i(\ell_i+1)}{2r^2}-\frac{Z}{r}-\frac{k_i^2}{2}\right)F_{ij}(r)$$

$$+\sum_k V_{ik}(r)F_{kj}(r)=0. \tag{2}$$

The residual charge Z is equal to the net charge on the ion, and the potential V_{ik}, in the absence of the radiative optical potential, takes the simplified form

$$V_{ik}(r)=\sum_{\lambda=1}^{\lambda_m}\frac{C_{ik}^\lambda}{r^{\lambda+1}} \quad , \tag{3}$$

where the C_{ik}^λ are long-range potential coefficients. Perturbative methods are used to solve this equation at every energy E [23–25]. The zeroth order solutions are obtained by neglecting the interaction potential V_{ij}, yielding Coulomb functions. For open channels ($k_i^2/2>0$), the regular $[s_i(r)]$ and irregular $[c_i(r)]$ Coulomb functions are linearly independent solutions to these equations. For closed channels ($k_i^2/2<0$), on the other hand, the physically allowed solutions are given by the exponentially decreasing function [26]

$$\theta(r)=r^\nu e^{-Zr/\nu}\sum_n B_n r^{-n} \quad . \tag{4}$$

Here ν is the effective quantum number defined by $k^2=-Z^2/\nu^2$, the coefficients B_n are computed by standard asymptotic recurrence relations, and the overall normalization is such that $\int_{r_a}^\infty \theta^2(r)dr=1$. Another quantity of interest which is easily computed from Eq. (4) is the energy derivative of $\theta(r)$:

$$\theta'(r)=\frac{d\theta(r)}{dE} \quad . \tag{5}$$

The zeroth-order solution matrix $F_{ij}(r)$ has n_t rows and n_o columns, where n_t is the total number of channels, and n_o is the number of open channels. It can be written as

$$\mathbf{F}(r)=\begin{pmatrix}\mathbf{s}(r)+\mathbf{c}(r)\mathbf{K}_{oo}\\ \theta(r)\mathbf{K}_{co}\end{pmatrix} \quad , \tag{6}$$

which defines the physical reactance matrix $\mathbf{K}_{oo}$. The first-order solutions are obtained using standard Green's function techniques [23,26]:

$$\mathbf{F}^{pert}(r)=\mathbf{F}(r)+\int_{r_a}^\infty \mathbf{G}(r,r')\mathbf{V}(r')\mathbf{F}(r')dr' \quad . \tag{7}$$

The Green's function takes the form

$$\mathbf{G}(r,r')=\begin{pmatrix} \mathbf{c}(r)\mathbf{s}(r')-\mathbf{s}(r)\mathbf{c}(r') & 0 \\ 0 & \theta'(r)\theta(r')-\theta(r)\theta'(r') \end{pmatrix}. \tag{8}$$

For the particular case of a diagonal potential, each closed-channel solution $\theta(r)$ is perturbed as follows:

$$\theta^{pert}(r_a)=\theta(r_a)\left(1-\int_{r_a}^{\infty}dr'\,\theta'(r')V(r')\theta(r')\right)+\theta'(r_a)\int_{r_a}^{\infty}dr'\,\theta(r')V(r')\theta(r') \ . \tag{9}$$

One appealing aspect of using θ and θ' is that they are both exponentially decaying functions at large r, so the integrals appearing in Eq. (9) are well behaved. The regular and irregular Coulomb functions for closed channels, on the other hand, diverge exponentially as $r\rightarrow\infty$, and therefore give rise to numerical problems in evaluating the integrals in Eq. (7).

When the closed-channel energy becomes small, however, the radius at which Eq. (4) can be used to evaluate the $\theta(r)$ and $\theta'(r)$ functions diverges, and so the regular and irregular functions are used instead. From these, the exponentially converging and diverging functions

$$e^{-}(r)=\left(\frac{\pi\nu^3}{2}\right)^{-1/2}[s(r)\cos\pi\nu-c(r)\sin\pi\nu], \tag{10}$$

$$e^{+}(r)=\left(\frac{\pi\nu^3}{2}\right)^{1/2}[c(r)\cos\pi\nu+s(r)\sin\pi\nu] \tag{11}$$

replace $\theta(r)$ and $\theta'(r)$. They are evaluated at $r=r_a$, and integrated outward to a sufficiently large radius that the perturbation integrals are nearly converged yet the diverging behavior of the $e^{+}(r)$ function is not problematic [27]. We emphasize that this alternate method is only used near the Rydberg limit, typically for effective quantum numbers $\nu>50$. We now discuss how various types of damping phenomena are treated within the R-matrix method.

A. Inner-region damping

The first type of damping included, which will be referred to as inner-region damping, is that for which the final decay state is entirely contained within the R-matrix box ($r\leq r_a$). Inner-region damping is accounted for by modifying the R matrix as a result of the optical potential for this decay, which vanishes outside the box ($r>r_a$). The size of the R-matrix box is chosen so as to completely contain the target orbitals; the resulting collision strengths are not sensitive to this choice since long-range potentials are included outside this region. The optical potential, in the length gauge, takes the form [16]

$$V_{rad}=-i\sum_b \frac{2\omega_b^3}{3c^3}D|b\rangle\langle b|D \ , \tag{12}$$

where $\omega=E-E_b$ is the energy difference between energies of the scattering and final states, $D=\sum_{s=-1}^{s=1}r_sC_s^1$ is the dipole operator, C_m^{λ} is the renormalized spherical harmonic $C_m^{\lambda}=\sqrt{4\pi/(2\lambda+1)}Y_m^{\lambda}$, and $|b\rangle$ represents a normalized final state. This potential contributes an additional term to the Hamiltonian matrix:

$$H_{\alpha\alpha'}\rightarrow H_{\alpha\alpha'}-i\sum_b \frac{2\omega_b^3}{3c^3(2J+1)}\langle\alpha||r||b\rangle\langle b||r||\alpha'\rangle \ , \tag{13}$$

where J is the total angular momentum of the scattering-state symmetry. We run the R-matrix codes in their photoionization mode in order to produce dipole matrix elements $D_{\alpha\beta}$ between basis functions of the initial (α) and final (β) symmetries. The program STGB [23] is run in order to compute the expansion coefficients a_β of the wavefunction $|b\rangle$:

$$|b\rangle=\sum_\beta a_\beta|\beta\rangle \ . \tag{14}$$

The reduced dipole matrix element in Eq. (13) can then be computed as

$$\langle\alpha||r||b\rangle=\sum_\beta D_{\alpha\beta}a_\beta \ . \tag{15}$$

The effect of adding an imaginary potential to the Hamiltonian is to modify the R matrix as [16]

$$R=W\frac{1}{\epsilon-E}W^T-W\frac{1}{\epsilon-E}X \times\left[\frac{X^T\frac{1}{\epsilon-E}X}{1+\left[X^T\frac{1}{\epsilon-E}X\right]^2}\right]X^T\frac{1}{\epsilon-E}W^T \tag{16}$$

$$+iW\frac{1}{\epsilon-E}X\left[\frac{1}{1+\left[X^T\frac{1}{\epsilon-E}X\right]^2}\right]X^T\frac{1}{\epsilon-E}W^T \ . \tag{17}$$

Here the array X is given by

$$X_{\alpha b}=\sum_\beta \sqrt{\frac{2(E-E_b)^3}{3c^3(2J+1)}}\langle\alpha||r||\beta\rangle a_\beta \ . \tag{18}$$

Since the continuum orbitals are still constructed from the same model potential, we use the same form of the Buttle

correction for this new complex Hamiltonian as is used for an unmodified, real Hamiltonian. It should be noted that construction of the R matrix requires a matrix inversion at every energy. However, the matrix inverted has a rank equal to the number of final bound wave functions, n_b, and not the size of the total basis. Nevertheless, even the inversion of this smaller matrix can lead to a substantial increase in computational time.

B. Type I damping

The second type of damping is the result of a core transition, i.e., it has the form

$$\mathcal{A}\Phi_i\theta_{n\ell}\rightarrow\mathcal{A}\Phi_f\theta_{n\ell}+\hbar\omega \ , \tag{19}$$

where Φ_i and Φ_f are the initial and final target states connected by the usual selection rules, $\theta_{n\ell}$ is the valence orbital for an outer-region electron with principle quantum number n and angular momentum l, $\mathcal{A}$ is an antisymmetrizing operator, and a photon is emitted with energy $\hbar\omega=E_i-E_f$. This damping is included by modifying the binding energy of the valence orbital $\theta_{n\ell}$ [16]:

$$\epsilon_{n\ell}\rightarrow\epsilon_{n\ell}-\frac{i}{2}\sum_f \Gamma_{i\rightarrow f} \ . \tag{20}$$

In this equation, $\Gamma_{i\rightarrow f}=A_r(i\rightarrow f)$ is the radiative width of the core transition which can be computed from the long-range dipole potential to be [19]

$$A_r(i\rightarrow f)=\sum_{\ell_i,\ell_j}\frac{\omega^3(2J+1)(C^1_{\ell_i\ell_j})^2}{c^3W^2(K_i,K_j,\ell_i,\ell_j;1,J)(2K_i+1)\max(\ell_i,\ell_j)} \ . \tag{21}$$

Here K_i refers to the angular momentum of the target J_i coupled to the spin $s_i=1/2$ of the colliding electron, J is the total angular momentum, the W are Racah coefficients, and $C^1_{\ell_i\ell_j}$ is the long-range dipole potential coupling channel ℓ_i to channel ℓ_j. The orbitals θ are evaluated using standard asymptotic expansions. The energy can be modified by simply substituting the complex energy for the real energy when evaluating the function $\theta_{n\ell}$ [26]. The result is to produce the complex functions θ_c and θ_c'. An alternate method is to use quantum-defect methods and replace the threshold energy for the closed channel with a complex threshold energy, although this method can not accurately account for long-range potentials, which effect the mixing of closed-channel orbitals.

In calculating the perturbed solutions, we neglect the complex energy in evaluating the long-range integrals, but include it in the zeroth-order solutions themselves:

$$\theta_c^{pert}(r_a)=\theta_c(r_a)\left(1-\int_{r_a}^{\infty}dr'\,\theta'(r')V(r')\theta(r')\right)+\theta_c'(r_a)\int_{r_a}^{\infty}dr'\,\theta(r')V(r')\theta(r') \ . \tag{22}$$

Thus we have a way of including both type I damping and the long-range potentials in the outer-region solutions.

We can also include this type of damping when using the alternative solutions $e^-(r)$ and $e^+(r)$. If no long-range potentials are included, and the solutions $s(r)$ and $c(r)$ are insensitive to small changes in the energy, then the solutions are obtained by just using $\cos(\pi\nu_c)$ and $\sin(\pi\nu_c)$, where $\nu_c=1/\sqrt{(1/\nu^2-i\Gamma/2)}$. The resulting S matrix obtained by using these modified functions can be written using quantum-defect theory as [16]

$$S=S_{oo}-S_{oc}(S_{cc}-e^{-2\pi i\nu_c})S_{co} \ . \tag{23}$$

However, this alternate method of treating outer-region perturbations assumes slow variance of the solutions $s(r)$ and $c(r)$ with respect to energy [27], which is only true for high ν, and thus this method is inappropriate for including outer-region perturbations for low and intermediate resonances.

It must be pointed out that the type I damping potential actually exists in both the inner and outer regions, so that the inner-region solutions should be modified as well. For high n, $\theta_{n\ell}$ is essentially zero inside the R-matrix box, and so the damping potential can be neglected. However, for lower n, a significant portion of the valence-electron wave function resides in the inner region. Thus the final decay state on the right-hand side of Eq. (19) must be included in the inner-region optical potential of Eq. (12). If quantum-defect methods are used to include type I damping, on the other hand, these inner-region decay states do not have to be included. This is because the effect of using the complex ν_c in Eq. (23) is to modify the target thresholds in both the inner and outer regions. Although such ambiguity between inner and outer region damping does not arise in the present case of Ti^{20+}, we have studied other systems for which we verified that, when modifying the $\theta_{n\ell}$ functions, inner decay states also had to be included in order to obtain results identical to those using Eq. (23) alone.

C. Type II damping

Type II damping is the result of a valence transition:

$$\mathcal{A}\Phi_i\theta_{n\ell}\rightarrow\mathcal{A}\Phi_i\theta_{n'\ell\pm1}+\hbar\omega \ , \quad n'<n \ . \tag{24}$$

To include this type, we have utilized a distorted-wave approximation to perturb the outer-region solutions:

$$\theta^{pert}(r_a)=\theta(r_a)+\theta'(r)\int_{r_a}^{\infty}dr'\,\theta(r')V_{opt}(r,r')\theta(r') \tag{25}$$

$$=\theta(r_a)-i\sum_{n'}\frac{\Gamma_{n\ell\rightarrow n'\ell\pm1}}{2}[\theta'(r)] \ , \tag{26}$$

where $\theta'(r)\equiv d\theta(r)/dE$. We make use of the fact that the potential is spherically symmetric, and so does not couple between various closed channels. The width Γ is calculated in the hydrogenic approximation

$$\Gamma_{n\ell\to n'\ell'}=\frac{4\omega^3}{3c^3(2J_c+1)}|\langle n\ell||r||n'\ell'\rangle|^2 \ . \quad (27)$$

The bra $|n\ell\rangle$ refers to the hydrogenic wave function $P_{nl}(r)$.

D. Distorted-wave method

We used perturbative methods for the resonance contributions to electron-impact excitation via the computer program AUTOSTRUCTURE [28]. These were added to background cross sections from two-state Breit-Pauli R-matrix calculations. By modifying the total width of each resonance, radiative damping is included [10]:

$$\Gamma_i^{tot}=\sum_j \Gamma_{i\to j}^a+\sum_k \Gamma_{i\to k}^r \ . \quad (28)$$

Here $\Gamma_{i\to j}^a$ is the width for autoionization from the resonant state i to a continuum state j, and $\Gamma_{i\to k}^r$ is the radiative width for decay to a final bound state k.

The calculations were done in one of two modes. In the first, the resonances were treated as isolated, and thus described by a single distorted-wave valence orbital coupled to a target state. This enables the determination of the resonance contribution for each set of quantum numbers $n\ell$, and is computationally efficient. In the second mode, configuration interaction between all such isolated states within a certain energy range was allowed. This takes into account what is expected to be the dominant interference mechanism [6]. However, inclusion of CI at the Rydberg limit becomes impractical due to the infinite number of resonances in this energy range.

III. RESULTS

The test case chosen is electron-impact excitation in Ti^{20+}. The target orbitals $\{1s,2s,2p,3s,3p,3d\}$ were generated from the multiconfiguration Hartree-Fock (MCHF) computer package of Froese Fischer [29]. The energies of the first 17 target levels, which are numbered for easier identification, are listed in Table I. The experiment [17] measured the x-ray emission of the $\{Z,Y,X,W\}$ lines, corresponding to excitations of levels {2,4,6,7}, respectively, with radiative redistribution taken into account. That is, the actual reported experimental cross sections below the $n=3$ thresholds are measurements of the x rays emitted from certain $n=2$ excited states. One has to consider the probability that a higher-lying $n=2$ state might be populated and radiatively decay to a lower $n=2$ state rather than decaying to the ground state. By factoring in these branching ratios [17], the experimental cross sections can be related to the present theoretical excitation cross sections by

$$\sigma_Z=\sigma_{1\to 2}+(0.872)\sigma_{1\to 3}+(0.3)\sigma_{1\to 6}, \quad (29)$$

$$\sigma_Y=\sigma_{1\to 4}, \quad (30)$$

$$\sigma_X=(0.7)\sigma_{1\to 6}, \quad (31)$$

TABLE I. Ti^{20+} levels and energies.

No.	Transition	Level		Energy (eV)
1		$1s^2$	$^1S_0$	0.0
2	Z	$1s2s$	$^3S_1$	4706.0
3		$1s2p$	$^3P_0$	4728.5
4	Y	$1s2p$	$^3P_1$	4730.8
5		$1s2s$	$^1S_0$	4732.3
6	X	$1s2p$	$^3P_2$	4738.1
7	W	$1s2p$	$^1P_1$	4755.0
8		$1s3s$	$^3S_1$	5573.1
9		$1s3p$	$^3P_0$	5579.3
10		$1s3s$	$^1S_0$	5579.8
11		$1s3p$	$^3P_1$	5579.9
12		$1s3p$	$^3P_2$	5582.0
13		$1s3d$	$^3D_1$	5585.6
14		$1s3d$	$^3D_2$	5585.7
15		$1s3p$	$^1P_1$	5586.5
16		$1s3d$	$^3D_3$	5586.5
17		$1s3d$	$^1D_2$	5586.7

$$\sigma_W=\sigma_{1\to 7} \ . \quad (32)$$

Above the $n=3$ thresholds, additional cascade effects must be considered, but in the present study we will focus only on the resonance structure below these thresholds.

We use the Breit-Pauli R-matrix method [21,22] to study these excitations. As a check on the validity of using this semirelativistic approximation, we also used the fully relativistic R-matrix package of Norrington [30,31] and found excellent agreement between the two results when radiation damping was omitted. We could not include radiation damping in the fully relativistic method since dipole matrices are not presently calculated in that code. Also, fully relativistic calculations required much more computational time.

A. R-matrix calculations with and without radiative damping

We show the R-matrix results from calculations with and without damping in Fig. 1 for the Y transition. According to Table I, the highest $n=2$ target level is $1s2p\ ^1P_1$ at 4755 eV. Resonances attached to this state are expected to dominate all others since they are captured via a dipole-allowed core excitation. We see, first of all, that the undamped cross sections show large resonance enhancements below 4755 eV due to the complete Rydberg series accumulating at the $1s2p\ ^1P_1$ threshold. This feature is completely absent, however, in the damped results, indicating that within the manifold of $n=2$ target thresholds (KLn resonances), there is tremendous damping of resonances. At about 5000 eV, there are resonance features due to the $1s3\ell3\ell'$ configuration (KMM resonances), and at 5250 eV there are KMN ($1s3\ell4\ell'$) resonances, neither of which show noticeable damping. However, as the principal quantum number increases, we see evidence of increased damping of the KMn resonances up until the final $n=3$ threshold at 5560 eV. This clearly shows that R-matrix calculations without radiative damping produce erroneously large resonance features and are therefore inaccurate.

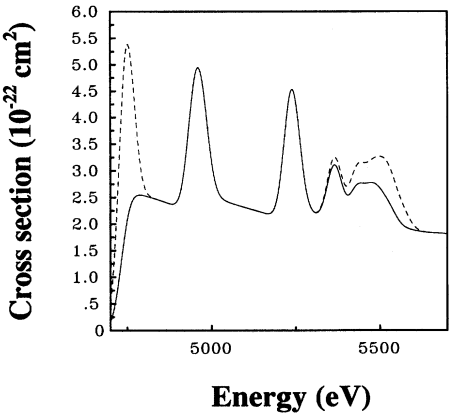

FIG. 1. Electron-impact excitation cross section for the $1s^2(^1S_0)\rightarrow 1s2p(^3P_1)$ (Y) transition in Ti^{20+}. Results are from a 17-level R-matrix calculation, convoluted with a 50 eV FWHM Gaussian. Solid line: radiative damping potential included; dotted line: no radiative damping.

We focus on the region between the $n=2$ thresholds. The resonances in this region are due to capture into the $1s2\ell n\ell'$ configurations. The range of n values can be estimated by the following quantum-defect formula:

$$E_{resonance}=E_{threshold}-Z^2/2n^2 \ , \tag{33}$$

to be $10\leq n<\infty$. The largest resonances are expected to be those for which a valence electron is attached to a dipole-allowed core state. These also are strongly damped since the $\Delta n=1$ core transition has a large energy difference ω. Recall that the autoionizing width for a resonance of the form $1s2p(^1P_1)n\ell\rightarrow 1s2s(^3S_{0,1})\epsilon\ell'$ scales like $1/n^3$, whereas the radiative width for the core transition $1s2p(^1P)n\ell\rightarrow 1s^2(^1S)n\ell+\hbar\omega$ is independent of n. We therefore expect the radiative rate to dominate, and subsequently completely damp the resonance, as $n\rightarrow\infty$. For the present case, it is apparent that for $n>10$, sufficient damping exists, and the resonance contribution goes to zero as $n\rightarrow\infty$. We highlight the energy region between the $n=2$ thresholds in Fig. 2 in an unconvoluted plot, and it is seen that the resonances do become completely damped in this region.

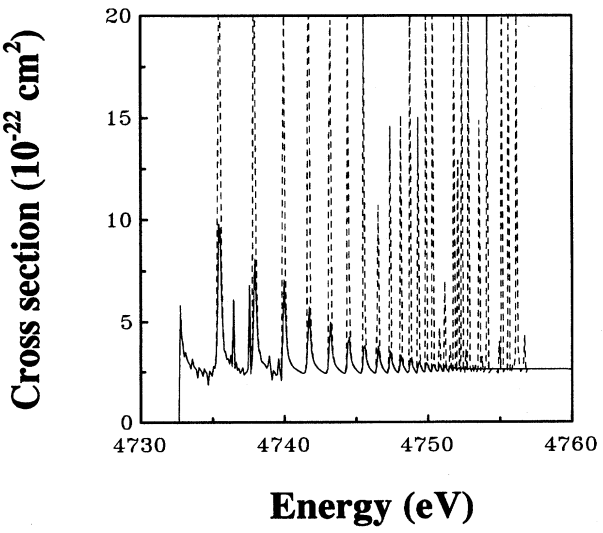

FIG. 2. Same as Fig. 1, except with no convolution.

It should be pointed out that a study of the damping of these resonances had been performed on He-like oxygen by Seaton and co-workers [14,15] using quantum-defect methods [24] to incorporate radiation effects [4]. They noticed similar damping of these resonances for higher n as well. However, their implementation of the quantum-defect method did not allow for perturbations of the outer-region solutions, which, in general, is necessary in order to obtain the correct resonance widths.

For the present calculations we found that the resonance profile did not require outer-region perturbations except near the Rydberg limit $n\rightarrow\infty$, at which point the resonances themselves are completely damped. Thus, the methods used by Pradhan and Seaton are completely valid for the treatment of type I damping in the current system. That outer-region perturbations are unnecessary can be understood in the following way. The capture rate from the ground-state continuum to the resonant state is proportional to a Slater integral involving the valence orbital $\theta_{nl}(r)$ and a continuum orbital $\epsilon_{kl}(r)$. The continuum orbital has such a large channel energy ($k^2\sim 360$ Ry) that it oscillates rapidly outside the R-matrix box, whereas the valence orbital oscillates slowly. Thus, the outer-region contribution to this Slater integral is negligible. The autoionization rate from the resonances to the excited continua are not affected by long-range potentials, either. This is because the resonances are mostly due to the $1s2p\ ^1P_1n\ell$ configuration, whereas the excited states are all triplet states (except for the W excitation, $1s2p\ ^1P_1$, which is above these resonances) so the only coupling is through the short-range exchange potential.

In summary, we find that the KLn resonances are completely damped, the KMM and KMN resonances are not damped at all, and the KMn resonances for $n>4$ begin to show increasing damping up until the limit $n\rightarrow\infty$, where complete damping occurs. In these calculations using the optical potential, all types of damping were included. However, inner-region damping, which occurs only for the KMM resonances, is negligible. Type II damping was found to be much weaker than the type I damping for the KLn resonances, and the KMn resonances do not decay by type II damping since there are no KLn' bound states. Almost the same results for Ti^{20+} could have been obtained including only type I damping.

B. Distorted-wave results with and without CI between resonances

We also performed distorted-wave calculations for this excitation cross section. First, we repeated the method of calculation used in the EBIT study [18], but used a Breit-Pauli, rather than Dirac, Hamiltonian. This method allowed for CI between all KMM $(1s3\ell 3\ell')$ resonances, but treated all higher-lying $(1s3\ell n\ell')$ resonances as isolated, and so permitted no CI between these. We found that our results were quite similar to the previous calculations [18]. In

a second distorted-wave calculation, we also allowed CI between all $1s3\ell 3\ell'$ and $1s3\ell 4\ell'$ resonances. Both of these results are shown in Fig. 3 along with the radiation-damped R-matrix calculations. We see that the KMM feature has been reduced somewhat by including the additional CI. However, there is a marked enhancement of the KMN feature due to the additional CI, which brings this feature into good agreement with the R-matrix results. We also see that the higher $1s3\ell n\ell'$, $n>4$, resonance features, which are treated as isolated, are less pronounced than the R-matrix results. This difference persists up to the Rydberg limit. Thus we conclude that CI is important along the whole sequence and is the principal shortcoming of the distorted-wave method. Again, both R-matrix and distorted-wave methods include radiation damping.

We finally point out that there is a certain amount of interference between resonances and the background, as evidenced by the asymmetric profiles. While this type of interference can also be included within the distorted-wave method in principle, no general scheme for doing so has been implemented. This is a minor shortcoming, since this asymmetric component thermally averages to zero, but for detailed comparison with experiments at high resolution, this type of interference may be needed.

C. Theory vs experiment

We now compare the final R-matrix results for all four excitations to the EBIT experiment in Fig. 4. In these final calculations, all radiation damping is included as well as the outer-region perturbations due to the long-range dipole and quadrupole potentials. We first point out that the enhanced KMN features, which we have attributed to CI between resonances, bring theory into better agreement with experiment than previous distorted-wave results [18]. The higher-lying resonances also seem to be brought into better agreement with experiment. One discrepancy that still exists is that the lower-energy features, especially the KMM resonances, are narrower but higher than experiment. This might be due to our convoluting with a 50 eV full width at half maximum

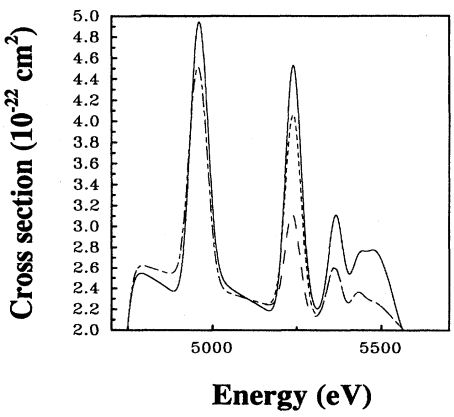

FIG. 3. Electron-impact excitation cross section for the $1s^2(^1S_0)\rightarrow 1s2p(^3P_1)$ (Y) transition in Ti^{20+}. Solid line: R-matrix results; dotted line: IPIRDW results with CI between all KMM and KMN resonances; dash-dotted line: IPIRDW results with CI between all KMM resonances only.

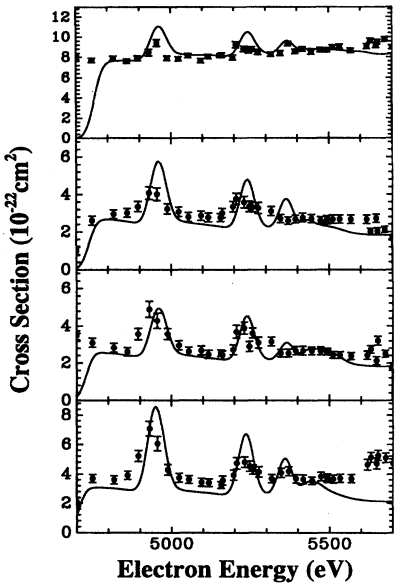

FIG. 4. R-matrix results for the electron-impact excitation cross section in Ti^{20+}: (a) $1s^2(^1S_0)\rightarrow 1s2p(^3S_1)$ (Z) transition; (b) $1s^2(^1S_0)\rightarrow 1s2p(^3P_1)$ (Y) transition; (c) $1s^2(^1S_0)\rightarrow 1s2p(^3P_2)$ (X) transition; (d) $1s^2(^1S_0)\rightarrow 1s2p(^1P_1)$ (W) transition. Experimental results from the EBIT experiment [13] are shown as solid circles.

(FWHM) Gaussian, which was the estimation of the experimental beam width [17]. A broader actual beam width would explain this difference. The W and Y cross sections also have some extra features in the near-threshold region that are not found theoretically, but this has been attributed to satellite lines, originating from dielectronically recombined states, which are indistinguishable from the dipole-allowed lines [17]. In the $n=3$ threshold region, we have omitted cascade effects from these states, and also we have not accounted for resonances of the form $1s4\ell n\ell'$, so that there is a noticeable difference between theory and experiment here as well. We finally point out that asymmetric resonance features are noticeable in the theoretical cross sections. As the experimental resolution improves, inclusion of this type of interference will be necessary for a detailed comparison of theory and experiment.

IV. SUMMARY

We have demonstrated that the study of electron-impact excitation in highly charged Ti^{20+} requires the simultaneous inclusion of radiative-damping and interfering resonance effects. Thus, R-matrix codes for these calculations should include the radiative optical potential in the Hamiltonian. Distorted-wave methods, on the other hand, would need to be modified to include CI interference of entire Rydberg series of resonances, and perhaps to include interference with the background as well. As the experimental resolution becomes finer, these effects will become increasingly important for determining detailed resonance stucture in electron-ion excitation cross sections. Rate coefficients, which are obtained by thermally averaging these cross sections and are used to model laboratory and astrophysical plasmas, are thus

ultimately dependent on accurate resonance contributions as well.

ACKNOWLEDGMENTS

We would like to thank the members of the Iron Project for the use of their Breit-Pauli R-matrix programs. T.W.G. and M.S.P. were supported in part by the U.S. Department of Energy, Office of Fusion Energy, under Contract No. DE-FG05-86-ER53217 with Auburn University, F.R. was supported in part by a NSF Young Investigator Award, and N.R.B. was supported in part by EPSRC Contract No. GR/K/14346 with the University of Strathclyde.

[1] *Atomic Processes in Plasmas*, edited by W. L. Rowan, AIP Conf. Proc. No. 322 (AIP, New York, 1995).
[2] A. H. Gabriel and C. Jordan, in *Case Studies in Atomic Collision Physics II*, edited by M. R. C. McDowell and E. W. McDaniel (North-Holland, Amsterdam, 1972), p. 211.
[3] See, for example, K. M. Aggarwal, Astrophys. J. Suppl. **77**, 677 (1991).
[4] P. C. W. Davies and M. J. Seaton, J. Phys. B **2**, 757 (1969).
[5] U. Fano, Phys. Rev. **124**, 1866 (1961).
[6] D. C. Griffin, M. S. Pindzola, F. Robicheaux, T. W. Gorczyca, and N. R. Badnell, Phys. Rev. Lett. **27**, 3491 (1994).
[7] M. D. Hershkowitz and M. J. Seaton, J. Phys. B **6**, 1176 (1973).
[8] R. D. Cowan, J. Phys. B **13**, 1471 (1980).
[9] M. H. Chen, K. J. Reed, and D. L. Moores, Phys. Rev. Lett. **64**, 1350 (1990).
[10] N. R. Badnell, M. S. Pindzola, and D. C. Griffin, Phys. Rev. A **43**, 2250 (1991).
[11] P. G. Burke and W. D. Robb, Adv. At. Mol. Phys. **11**, 143 (1975).
[12] P. G. Burke and K. A. Berrington, *Atomic and Molecular Processes: An R-matrix Approach* (IOP Publishing, Bristol, 1993).
[13] K. Sakimoto, M. Terao, and K. A. Berrington, Phys. Rev. A **42**, 291 (1990).
[14] R. H. Bell and M. J. Seaton, J. Phys. B **18**, 1589 (1985).
[15] A. K. Pradhan and M. J. Seaton, J. Phys. B **18**, 1631 (1985).
[16] F. Robicheaux, T. W. Gorczyca, M. S. Pindzola, and N. R. Badnell, Phys. Rev. A **52**, 1319 (1995).
[17] S. Chantrenne, P. Beiersdorfer, R. Cauble, and M. B. Schneider, Phys. Rev. Lett. **69**, 265 (1992).
[18] M. H. Chen, published in reference [17] (1992).
[19] K. A. Berrington, W. B. Eissner, and P. H. Norrington, Comput. Phys. Commun. (to be published).
[20] D. G. Hummer, K. A. Berrington, W. B. Eissner, A. K. Pradhan, H. E. Saraph, and J. A. Tully, Astron. Astrophys. **279**, 298 (1993).
[21] N. S. Scott and P. G. Burke, J. Phys. B **13**, 4299 (1980).
[22] N. S. Scott and K. T. Taylor, Comput. Phys. Commun. **25**, 347 (1982).
[23] K. A. Berrington, P. G. Burke, K. Butler, M. J. Seaton, P. J. Storey, K. T. Taylor, and Yu Yan, J. Phys. B **20**, 6379 (1987).
[24] M. J. Seaton, Rep. Prog. Phys. **46**, 167 (1983).
[25] N. C. Sil, M. A. Crees, and M. J. Seaton, J. Phys. B **17**, 1 (1984).
[26] M. J. Seaton, J. Phys. B **18**, 2111 (1985).
[27] N. R. Badnell, D. C. Griffin, T. W. Gorczyca, and M. S. Pindzola, Phys. Rev. A **50**, 1231 (1994).
[28] N. R. Badnell, J. Phys. B **19**, 3827 (1986).
[29] C. Froese Fischer, Comput. Phys. Commun. **64**, 369 (1991).
[30] P. H. Norrington and I. P. Grant, J. Phys. B **14**, L261 (1981).
[31] P. H. Norrington and I. P. Grant, J. Phys. B **20**, 4869 (1987).